



Interaction between local corrosion and flow field of natural gas long-distance pipeline by artificial rectangular defect pit

Zhuo-wei Tan^{1,2} · Zhen-bo Wang¹ · Shu-yu Bai³ · Da-lei Zhang³ · Sheng-zhu Zhang⁴ · Frank Cheng⁵ · Shao-hua Xing⁶ · You-hai Jin¹

Received: 12 February 2021 / Revised: 14 April 2021 / Accepted: 15 June 2021 / Published online: 4 March 2022
© China Iron and Steel Research Institute Group 2022

Abstract

The corrosive environment in long-distance natural gas pipeline was simulated by the online high shear stress flow test platform. The interaction between flow fields and local corrosion in different local corrosion stages was studied by machining different depths rectangular defect pit (RDP) on X80 pipe steel specimens. The electrochemical signals of each specimen under high shear stress flow were measured online using an integrated three-electrode and electrochemical system. Raman spectroscopy confirmed that the corrosion scale of X80 pipeline steel in CO₂-saturated National Association of Corrosion Engineers solution was composed of FeCO₃. The scanning electron microscope images displayed variations in microstructure of the corrosion scale at different RDP depths and different areas. The flow field fluctuations induced by RDP were analyzed by computational fluid dynamics simulations and the development of local corrosion pits was discussed in terms of integrity of corrosion scale, convective mass transfer, and diffusion mass transfer.

Keywords CO₂ corrosion · Flow condition · Rectangular defect pit · Local corrosion · Corrosion electrochemistry

1 Introduction

The economic losses caused by corrosion in oil and gas transportation industries are considerable due to extensive use of carbon steel pipelines [1–4]. In natural gas transportation pipelines, it is particularly easy to produce

corrosion on carbon steel due to the presence of both condensate water and CO₂ [5–9]. Numerous studies have shown that the uniform corrosion in pipelines is a stable and slow process and does not affect the safety of operations [10, 11]. However, local corrosion occurs more often and there exists greater threat to safe operation of pipelines, especially in high-speed flow media [12–20]. The corrosion mechanism of carbon steel has been studied in carbon dioxide aqueous solutions [21, 22]. However, the flow fluid in pipelines rendered the corrosion process more complex, especially in terms of interactions between the corrosion and flow during the development of local corrosion. Therefore, it has great significance to study the development process of local corrosion for safe operation of gas and oil pipelines.

The occurrence of local corrosion would change the surface morphology of pipelines, leading to inhomogeneous local flow fields. Different from corrosion under stable flow field, locally produced uneven flow fields will result in locations with different corrosion characteristics. The fluctuation in flow field will directly affect the convection mass transfer process at the solid–liquid interface [23]. Meanwhile, the specific positions would be

✉ Da-lei Zhang
zhangdal2008@126.com

✉ You-hai Jin
jinyh@upc.edu.cn

¹ China University of Petroleum (East China),
Qingdao 266580, Shandong, China

² Xiangtan University, Xiangtan 411105, Hunan, China

³ School of Materials Science and Engineering, China
University of Petroleum (East China),
Qingdao 266580, Shandong, China

⁴ China Academy of Safety Science and Technology,
Beijing 100012, China

⁵ University of Calgary, Calgary, AB T2N 1N4, Canada

⁶ State Key for Marine Corrosion and Protection, Luoyang
Ship Material Research Institute,
Qingdao 266237, Shandong, China

mechanically affected by uneven flow fields, which can effectively destroy some formed corrosion scale, as well as affect the porosity and diffusion mass transfer processes [24, 25]. CO₂ corrosion of carbon steel produces iron carbonate (FeCO₃) mostly, and the dense FeCO₃ corrosion could slow down the corrosion process by preventing ions transfer between the solution and iron matrix effectively [26–28]. However, loose corrosion scale provides micro-channels for mass transfer to accelerate the corrosion process. On the other hand, total destruction of local corrosion scale and exposure of the matrix will accelerate the corrosion process of matrix. Therefore, the influence on corrosion process under flow would mainly include mass transfer, integrity, and porosity of corrosion scale.

Numerous studies have reported changes in mass transfer process caused by fluctuations in local flow field and established mass transfer models of related flow field parameters [29–33]. However, these studies on corrosion under flow conditions were carried out by conventional experimental apparatus mostly [22, 34–40]. The influence of fluid boundary layer at low flow rates will limit flow systems from forming strong wall shear stress on solid walls. Hence, it is hard to evaluate the wall shear stress on walls caused by local turbulence. To evaluate the effect of local turbulence accurately, the flow field fluctuation near solid–liquid interfaces need be strengthened.

In this work, X80 pipeline steel specimens with rectangular defect pit (RDP) were used to simulate local corrosion pits. The relationships between flow field parameters and local corrosion processes of vertical wall and bottom surfaces of RDP were analyzed. The corrosion tests were performed to improve thin liquid film channel of three-electrode system in National Association of Corrosion Engineers (NACE) solution. After the solution was deoxidized, CO₂ was purged until it was saturated. The corrosion was studied by online electrochemical measurements, including open circuit potential (OCP), electrochemical impedance spectroscopy (EIS), and linear polarization resistance (LPR). The composition of corrosion scale was detected by Raman spectroscopy and microstructures at different locations were observed by scanning electron microscopy (SEM). The flow field fluctuations induced by RDP were further analyzed by combining with computational fluid dynamic (CFD) calculations. The results revealed that different RDP depths induced variable flow fields, resulting in development of different regions and mechanisms of local corrosion.

2 Experimental

2.1 Setup

The flow system was composed of anti-corrosion plastic and the cooling system was made of 316L steel (Fig. 1) [38]. The test channel was made of plexiglass with size of 600 mm × 100 mm × 4.5 mm. The inlet and outlet of the channel were equipped with solution distribution box to ensure uniform distribution of solution in test channel (Fig. 2). The test port was located at test channel bottom and connected the integrated electrode by thread. The three-electrode system was arranged as equilateral triangular on the same plane with distance between the center of each electrode set to 15 mm (Fig. 3) [40]. The reference electrode and the counter electrode are arranged on the same side of the work electrode and parallel to the flow direction, to avoid the flow field of the work electrode surface from being interfered by other electrodes. During the experiments, the flow velocity was set to 5 m/s.

2.2 Materials and specimen preparation

To ensure consistent composition and metallurgical state of each specimen, all specimens were cut from the same piece of X80 pipeline steel. The chemical compositions are listed in Table 1. The specimens were cube-shaped with side length of 10 mm. RDP with depths of 0.3, 0.6, 0.9, 1.2 and 1.5 mm was machined on the test surface (Fig. 4). Before the experiments, the test surface was ground with 400, 600, 800 and 1000 grit sandpapers in sequence, then degreased with acetone and dried.

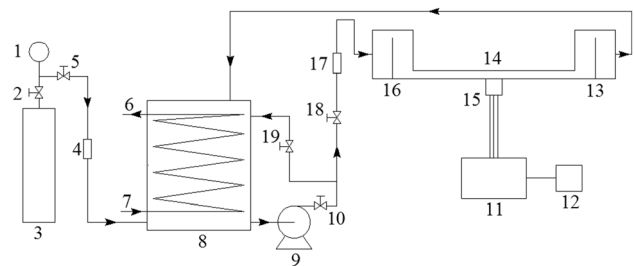


Fig. 1 Experimental setup. 1–CO₂ cylinder pressure meter; 2–CO₂ cylinder valve; 3–CO₂ cylinder; 4–gas flowmeter; 5–CO₂ flow valve; 6–cooling medium outlet; 7–cooling medium inlet; 8–solution container; 9–solution pump; 10–solution flow master valve; 11–electrochemical test system; 12–data storage computer; 13–rear solution distribution box; 14–test channel; 15–test electrode; 16–front solution distribution box; 17–solution flowmeter; 18–solution control valve; 19–solution return valve

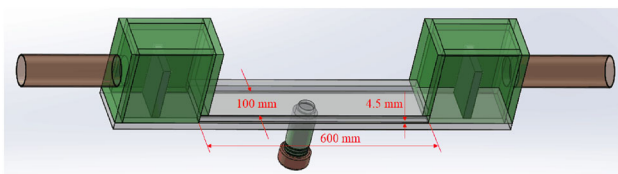


Fig. 2 Details of test channel

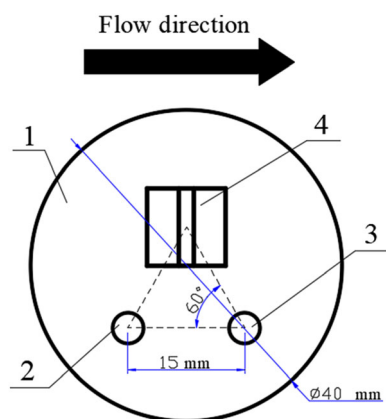


Fig. 3 Details of test channel and integral electrochemical probe. 1–Insulation material; 2–reference electrode; 3–counter electrode; 4–work electrode

To simulate condensate solution in natural gas transportation pipelines, corrosion test solution was used as recommended by NACE. The solution was made by dissolving 0.5 wt.% acetic acid and 5 wt.% sodium chloride in water, and then purged by CO_2 to CO_2 -saturation after deoxygenation with N_2 . The pH of the solution was kept at 2.7 ± 0.02 and temperature was set to 40 ± 1 °C under atmospheric pressure.

2.3 Electrochemical measurements

An integrated three-electrode system was used to achieve online testing under the dynamic flow system (Fig. 3). To this end, X80 pipeline steel specimen with RDP surface characteristic was employed as working electrode (WE), high purity zinc as reference electrode (RE), and platinum as counter electrode (CE). The electrochemical tests were performed on Solartron 1280C electrochemical workstation and each test lasted for 16 h. EIS measurements were obtained at 5 mV sinusoidal potential excitation and

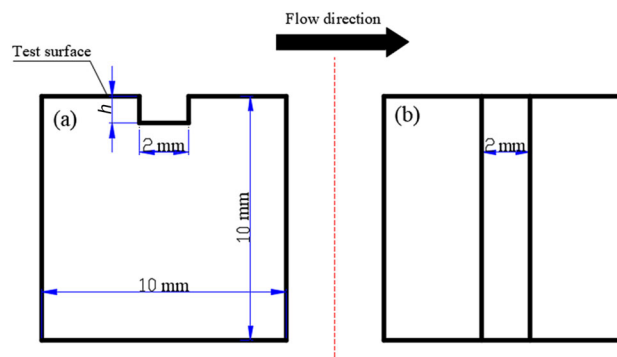


Fig. 4 Specification of RDP with flow direction. **a** Side view; **b** top view

frequencies from 1 to 10 mHz. LPR was obtained from -5 to 5 mV relative to OCP at scan rate of 0.01 mV/s.

2.4 Surface analysis

The micro-morphologies of specimens subjected to corrosion testing under flow were analyzed by SEM (FEI QUANTA FEG2500). Note that the iron matrix affected the detection results in regular component detection methods (X-ray diffraction and energy dispersive spectroscopy) due to the very thin aspect of corrosion scale. Therefore, compositions of corrosion scale were analyzed by Raman spectroscopy (Renishaw RM-3000) at wavelengths of 50 – 1600 cm^{-1} under He–Ne laser signal excitation of 10 μW and wavelength of 632.8 nm. The flow field induced by RDP varied with position. To detect corrosion scale of each RDP area, SEM test was performed by labeling.

2.5 Computation of flow field

The flow parameters near RDP were calculated by CFD (ANSYS FLUENT 15.0). A two-dimensional model of longitudinal cross-section of the testing channel with size of 600 mm \times 4.5 mm was built due to symmetry of flow field. RDP was located at the center of bottom of the testing channel. The grid measured 10 mm in length and centered on RDP of 0.025 mm \times 0.025 mm with grid size of both ends measuring 0.5 mm \times 0.025 mm. The fluid was considered as incompressible and the wall was considered as adiabatic. Standard k - ϵ with enhanced wall treatment

Table 1 Chemical composition of X80 pipeline steel (wt.%)

Mn	Si	Mo	C	Nb	V	Cr	Ni	Ti	P	S	Fe
1.83	0.28	0.22	0.063	0.061	0.059	0.03	0.03	0.016	0.011	0.0006	Balance

model was used for the simulations. The inlet was set as uniform velocity inlet (5 m/s) and outlet as outflow with standard atmospheric pressure of 0.1013 MPa. The simulations converged when residuals of all equations became stable and below 0.0001.

3 Results

3.1 Electrochemical measurements

EIS results of specimens with different RDP depths in CO₂-saturated NACE solution are depicted in Fig. 5. Note that specimens with different RDP depths induced various spectral characteristics. At RDP depths of 0.3, 1.2 and 1.5 mm, capacitive semicircle and inductive loop were identified at high and low frequencies, respectively. By comparison, two capacitive semicircles were observed at RDP depths of 0.6 and 0.9 mm. Thus, local defects at different depths had various effects on the corrosion of X80 pipeline steel under the flow.

The equivalent circuits and the fitting parameters are shown in Fig. 6. In the equivalent circuit, R_s represents the solution resistance, R_{ct} is the charge transfer resistance, L is the inductance, R_L is the inductive resistance, Q_{dl} is constant phase element (CPE) related to the double-layer capacitance, R_f is the resistance of corrosion scale, R_{df} is the resistance of dense film, and Q_f is CPE of corrosion scale [41]. Considering the inhomogeneity and roughness of the surface, Q_{dl} (constant phase angle element) was employed instead of ideal capacitance.

3.2 Corrosion rate

The corrosion rates of X80 steel specimens with different RDP depths were obtained by measuring and fitting the LPR test data. The polarization resistance (R_p) of the corrosion is given by [38]:

$$R_p = \frac{\Delta E}{\Delta I} \quad (1)$$

where ΔE and ΔI are the potential and current changes due to the input of the electrical signal. Based on the Stern-Geary equation, the corrosion current (I_{corr}) is given as follows:

$$I_{corr} = \frac{b_a b_c}{2.303(b_a + b_c)} \frac{1}{R_p} = \frac{B}{R_p} \quad (2)$$

where b_a and b_c are the Tafel constants; and B is the Stern-Geary constant, 18 mV. The corrosion rate (V_{corr}) can be calculated by:

$$V_{corr} = \frac{M I_{corr}}{n \rho F A} \quad (3)$$

where M is the molar mass of iron; n is the number of transferred electrons; ρ is the density of iron; F is the Faraday constant; and A is the surface area of the specimens.

As shown in Fig. 7, maximum corrosion rate was obtained at RDP depth of 0.3 mm. When the depths of RDP increased to 0.6 mm, the corrosion rates decreased significantly but slowly rose as depth continued to increase.

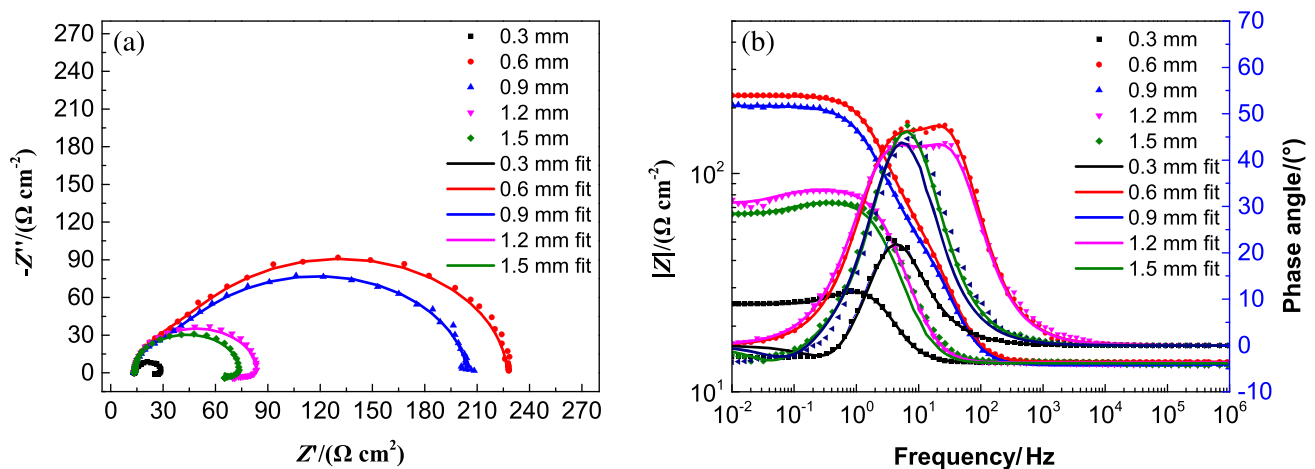


Fig. 5 EIS for specimens with different RDP depths. **a** Nyquist plots; **b** bode and $|Z|$ plots

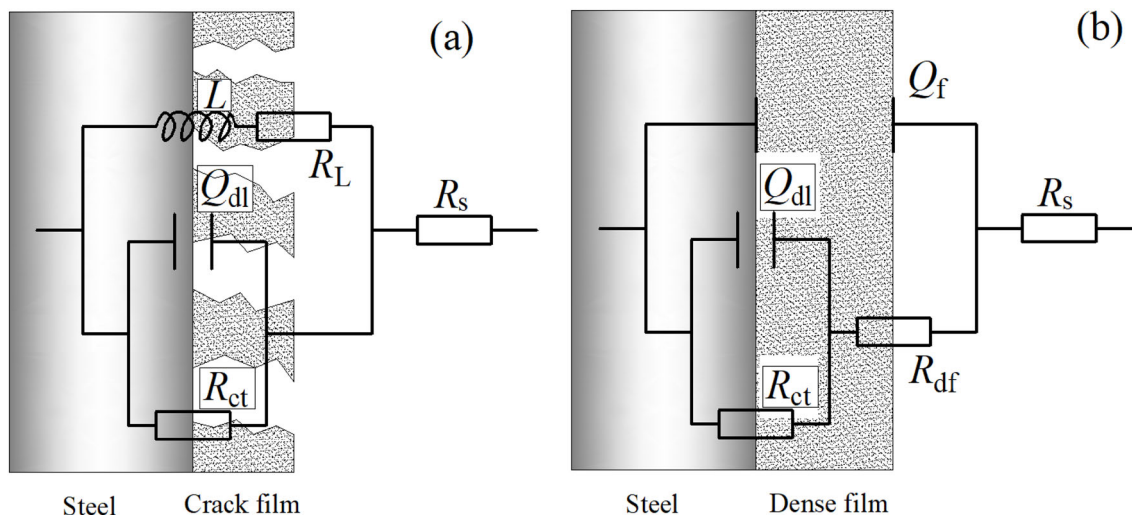


Fig. 6 Equivalent circuit for test impedance with different corrosion pit depths. **a** 0.3, 1.2, and 1.5 mm; **b** 0.6 and 0.9 mm

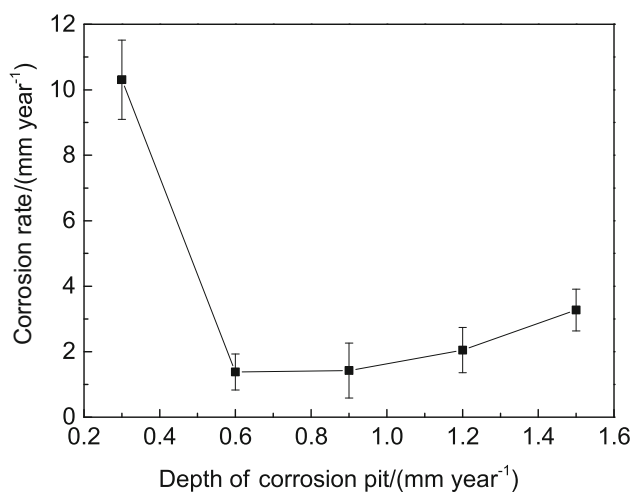


Fig. 7 Corrosion rate of X80 steel specimens with RDP (error bar represents standard deviation of three set tests under same conditions)

3.3 Corrosion scale microstructure and composition

After 16 h of corrosion testing under the flow, the microstructures of specimens were characterized by SEM and the results are illustrated in Fig. 8. Complete corrosion scale was exhibited on upstream of RDP. Hence, single wall shear stress could not sufficiently destroy dense and complete corrosion scale under 5 m/s flow. For specimens with 0.3 mm depth RDP, the corrosion scale in the pit and in its downstream looked obviously damaged by fluid flow. Complete corrosion scale formed in all areas of the tested surfaces with RDP depths of 0.6 and 0.9 mm. Specimens with RDP depths of 1.2 and 1.5 mm only in RDP area showed damaged corrosion scale, where complete corrosion scale formed at upstream and downstream of RDP. In

Fig. 9, the bands of Raman spectroscopy were consistent with siderite (FeCO_3) reported in the literature, confirming that corrosion scale was composed of FeCO_3 mainly [42–44].

3.4 Flow parameter calculation

The flow parameter distribution was simulated by CFD. The flow parameters in both horizontal and vertical directions near the wall were obtained for analyzing the reaction process occurring at solid–liquid interface. The parameters in horizontal direction near the wall are depicted in Fig. 10. The upstream distribution of Reynolds number (Re) for different RDP depths looked basically the same and displayed a peak in RDP. As RDP depth rose, the peak position moved backward and tended to be stable. The maximum Re was visible at turn point of RDP downstream. By comparison, another Re peak appeared in RDP downstream at 0.3 mm depth RDP. The wall shear stress (WSS) distribution in horizontal direction near the wall of different RDP depths appeared basically the same as that of Re . However, no WSS peak was visible at RDP downstream for 0.3 mm depth. The absolute pressure (ABP) distribution in the horizontal direction near the wall showed that maximum and minimum pressures of specimens with different RDP depths both appeared at turn point of RDP downstream. At RDP depth of 0.3 mm, the maximum pressure difference at turn point of RDP downstream reached 9000 Pa. As RDP depth increased, the pressure difference decreased and tended to be stable.

The flow field parameters of RDP upstream vertical wall are displayed in Fig. 11. Two Re peaks were observed and attributed to the turn point and the main reflux vortex in RDP. Three WSS peaks were noticed at RDP upstream

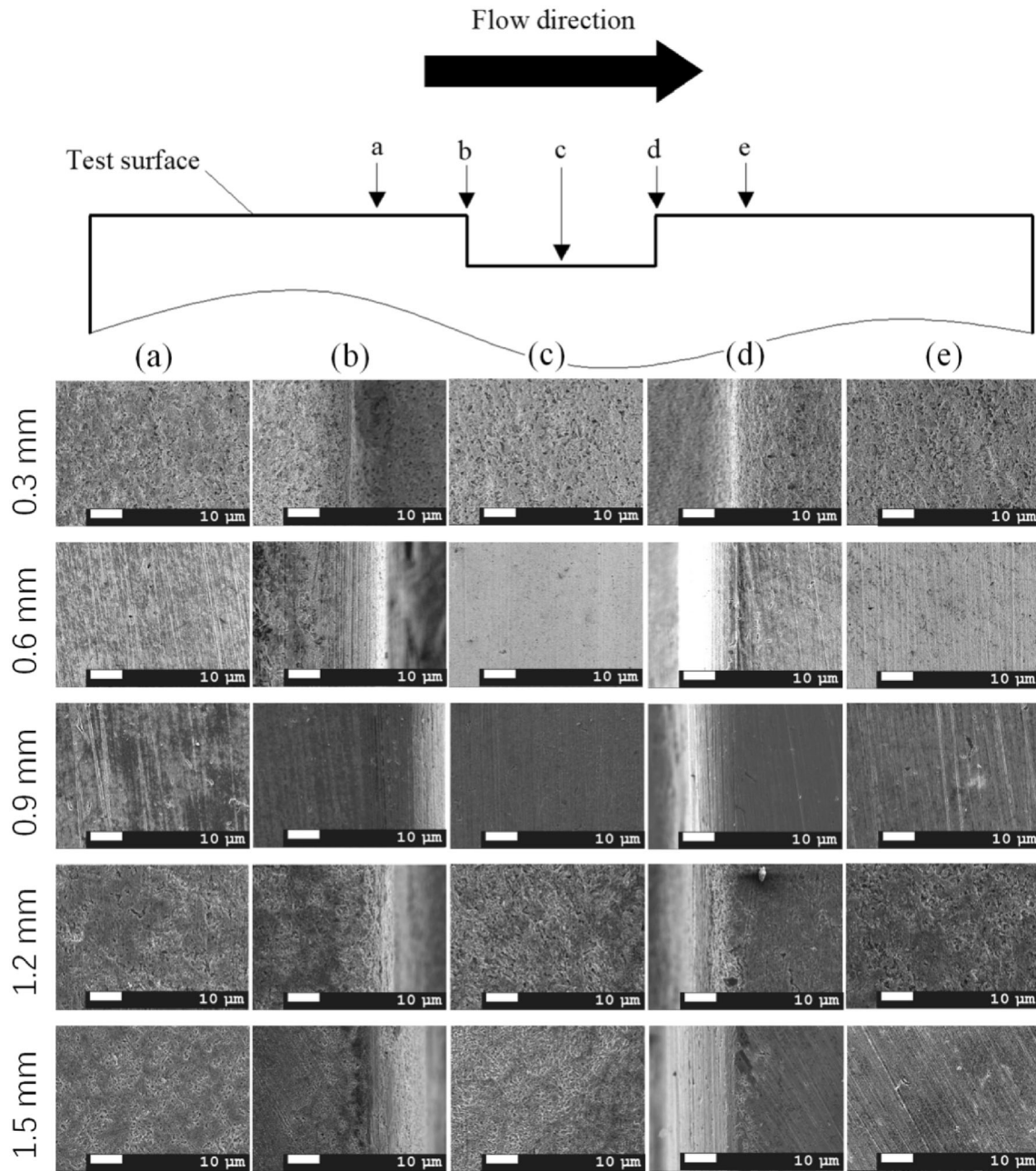


Fig. 8 SEM of corroded surface. **a** RDP upstream; **b** RDP upstream corner; **c** RDP bottom; **d** RDP downstream corner; **e** RDP downstream

vertical wall, attributed to the turn point, the main reflux vortex in RDP, and the small reflux vortex in the back-flow negative pressure zone. The absolute pressure distribution showed much lower value at RDP upstream vertical wall at depth of 0.3 mm when compared to those obtained with deeper RDP specimens. Overall, Re of RDP upstream vertical wall looked low, and the effect on corrosion scale was insufficient.

The flow field parameters of RDP downstream vertical wall are gathered in Fig. 12. As RDP depth rose, Re at RDP downstream vertical near-wall also rose gradually. For

specimens with fixed RDP depth, Re decreased with vertical depth. When RDP depth was above 0.9 mm, a Re peak with low intensity was recorded due to the small reflux vortex formed in the positive pressure region. WSS distribution showed two peaks at RDP vertical wall downstream. The first peak was located at turn point of RDP downstream and decreased with RDP depth. The second peak reflected the influence of fluid impact on the vertical wall downstream of RDP, where WSS rose rapidly with RDP depth and then tended to be stable. The absolute pressure on RDP downstream vertical wall decreased

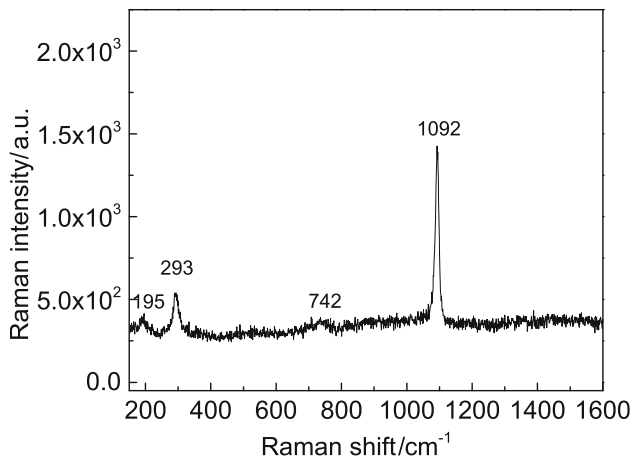


Fig. 9 Raman spectrum of corrosion scale and downstream of 0.3 mm RDP

rapidly with depth, and the shallow pit showed higher pressures in RDP downstream.

4 Analysis of flow affected local corrosion

4.1 Mechanism of reaction

The reaction mechanisms of steel–carbon dioxide corrosion have been investigated widely. Some studies revealed that the reaction mechanisms mainly depend on pH and temperature of the solution [9, 40, 45]. Here, pH of the corrosion solution was kept at 2.7 ± 0.02 at temperature of 40 °C. The cathodic reactions mainly included the reduction of hydrogen ions and carbonic acid according to Eqs. (4) and (5):

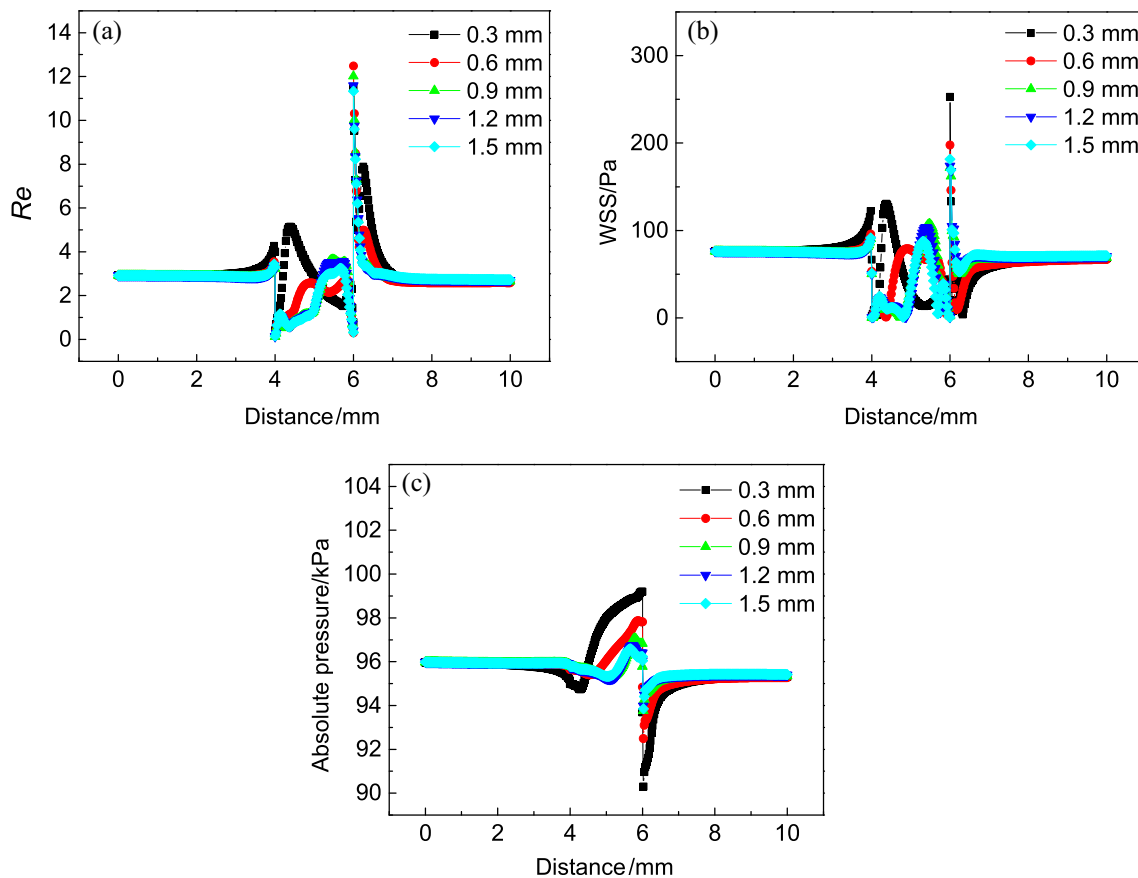


Fig. 10 Flow field parameters near-wall in direction of flow to horizontal direction. **a** *Re*; **b** WSS; **c** ABP

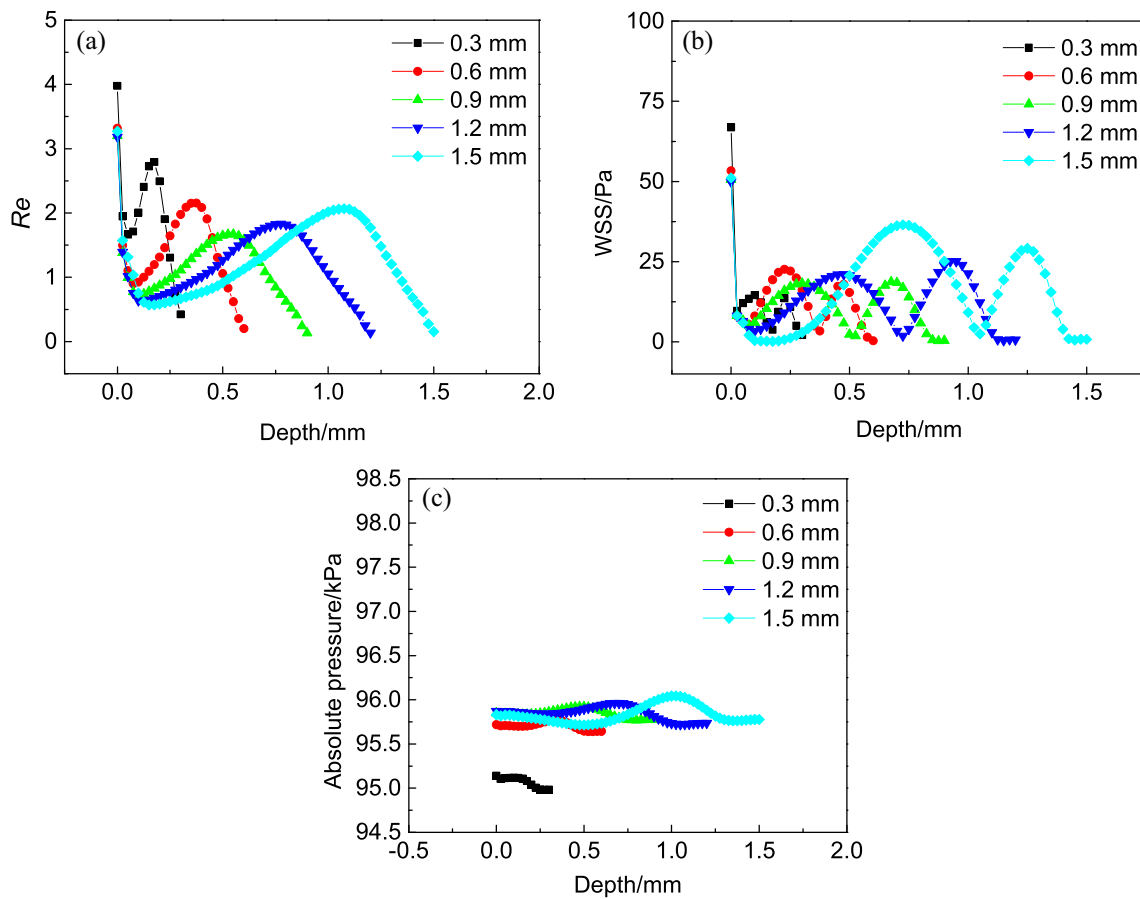
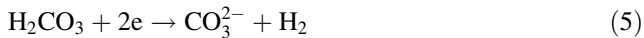
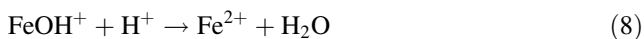
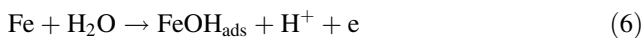


Fig. 11 Flow field parameters near vertical wall on upstream of RDP. **a** Re ; **b** WSS; **c** ABP

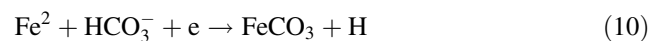
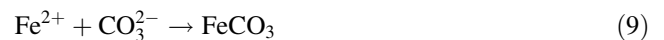


The anodic reaction would mainly consist of the iron dissolution following Eqs. (6)–(8):



The inductive loop shown at low frequencies in EIS corresponded to the adsorption and dissolution process of the intermediate products FeOH_{ads} [22], particularly for specimens with RDP depths of 0.3, 1.2 and 1.5 mm (Fig. 5). Hence, the matrix of X80 steel with these three RDP depths would always be in state of activation and dissolution during corrosion testing. Also, no complete and dense corrosion scale was formed on the test surface. The generated Fe^{2+} and CO_3^{2-} (or HCO_3^-) during the corrosion reaction led to excess FeCO_3 at the solid–liquid interface to reach super-saturation. Hence, some FeCO_3 was deposited on the test surface and other infiltrated into the bulk solution through diffusion and convection mass

transfer processes. The generation reaction of FeCO_3 could be expressed according to Eqs. (9) and (10) [18]:



Raman spectra showed that the corrosion scale was mainly composed of FeCO_3 , confirming the corrosion reaction of X80 steel in CO_2 -saturated NACE solution. The anodic reaction control step consisted of Fe dissolution, and cathodic reaction control step was based on diffusion of H^+ toward the solid–liquid interface. However, some studies reported that dense and complete FeCO_3 scale could hinder ion diffusion, preventing charge transfer between interfaces effectively [46]. Therefore, the integrity and denseness of the corrosion scale composed of FeCO_3 significantly impacted the corrosion process under flow conditions. Meanwhile, the influence of convective mass transfer during mass transfer process also played an important role in the corrosion process.

At RDP depths of 0.3, 1.2 and 1.5 mm, EIS (Fig. 5) and SEM (Fig. 8) data showed no formation of complete corrosion scale. Also, the damage position of the corrosion scale looked different from one specimen to another. By

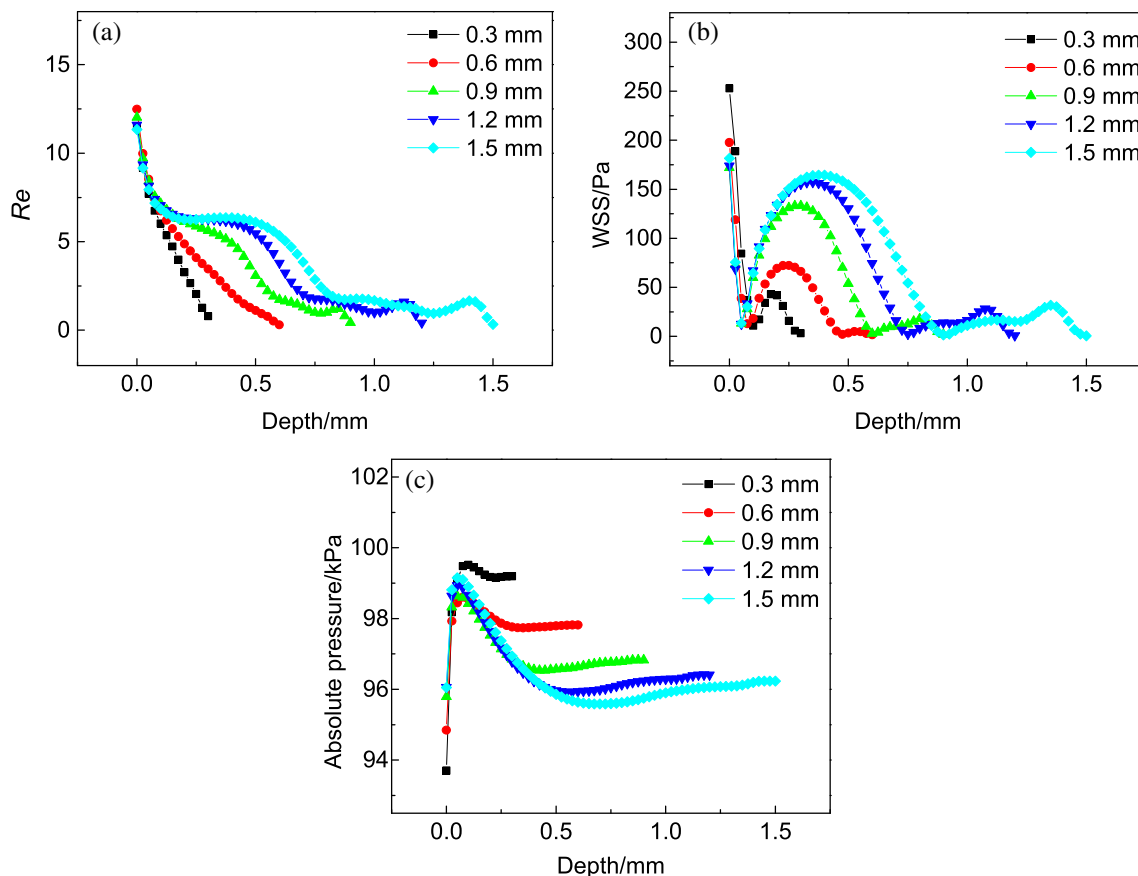


Fig. 12 Flow field parameters near vertical wall on downstream of RDP. **a** Re ; **b** WSS; **c** ABP

comparison, only the specimens with RDP depths of 0.6 and 0.9 mm formed complete corrosion scale. The corrosion rates obtained by LPR also confirmed rapid reduction in corrosion rates upon formation of complete corrosion scale, such as for specimens with RDP depths of 0.6 and 0.9 mm.

4.2 Mass transfer process

CO_2 corrosion of iron in CO_2 -saturated NACE solution can be summarized by two processes. The first one consisted of filtration of the reactive ions from the solution or corrosion scale to reach the iron matrix and participate in the corrosion reaction. The second process was the dissolution of iron matrix to yield Fe^{2+} , which will then be transported to the bulk solution or converted into FeCO_3 to deposit on the surface. Therefore, mass transfer process on corrosion process would have crucial influence.

4.2.1 Mass transfer of reactant

The reaction rate of medium transfer from the solution to reaction interface (metal surface) would determine the

corrosion reaction rate under the flow conditions. The limiting current densities of the electrochemical reactions caused by mass transfer of the reactant in the solution ($i_{\text{lim},j}$) can be written according to Eq. (11) [45]:

$$i_{\text{lim},j} = nFk_j(C_{b,j} - C_{s,j}) \quad (11)$$

where F is the Faraday constant; k_j is the mass transfer coefficient involved in reactant j ; and $C_{b,j}$ and $C_{s,j}$ are the concentrations of the reactant j in the bulk solution and at the reaction interface, respectively.

Note that $C_{s,j}$ can be calculated using the kinetics of charge transfer reaction. However, the data showed surface concentration of the reactant close to zero under pure mass transfer conditions. Hence, limiting current density can be expressed by:

$$i_{\text{lim},j} = nFk_jC_{b,j} \quad (12)$$

However, the convection mass transfer and the diffusion mass transfer under flow field simultaneously occur. The dimensionless Schmidt (Sc) and Sherwood (Sh) numbers were defined to link both the mass transfer processes and the influence of flow field parameters according to Eqs. (13) and (14):

$$Sc_j = \frac{\mu}{\rho D_j} = \frac{\nu}{D_j} \quad (13)$$

$$Sh_j = \frac{k_j l}{D_j} \quad (14)$$

where μ is the viscosity of solution; ρ is the density of solution; ν is the kinematic viscosity of the solution; l is the characteristic length of the test channel; and D_j is the diffusion coefficient of the reactant j in the solution.

When combined with limiting current density, Sh_j can be described by Eq. (15):

$$Sh_j = \frac{i_{lim,j}}{nFD_j C_{b,j}} \quad (15)$$

Therefore, Sh_j can be used to evaluate the corrosion reaction rate under the mass transfer process. Reported study suggested that Re , Sh_j and Sc_j can be described by Eq. (16) [47]:

$$Sh_j = aRe^b Sc_j^c \quad (16)$$

where a , b and c are constants related to the mass transfer process and obtained by experiment. Using Eq. (13), the dynamic viscosity and diffusion coefficient could be used to calculate Sc_j as independent flow parameter. Therefore, the intensity of mass transfer can be evaluated by the value of Re under the flow.

In Fig. 10a, the distribution of Re values in the horizontal direction near the wall showed basically stable at upstream and downstream of RDP. However, Re showed obvious local fluctuations under RDP, and different RDP sizes led to variable effects. As RDP depth rose, Re peak in the horizontal direction of RDP gradually moved backward, and the peak value gradually dropped to reach the same Re outside the plane of RDP. Therefore, the mass transfer process in horizontal direction near the wall surface of shallow pit was stronger than that in the deeper position. In addition, the mass transfer process looked mainly concentrated in front part of the shallow pit. As RDP depth developed, the mass transfer process in front part of horizontal direction of the pit obviously decreased, and rear part value became close to that of the plane out of RDP. Re peak at turn point of RDP downstream demonstrated the presence of strong mass transfer process. Meanwhile, Re peak value was present in downstream plane of the shallow pit (0.3 mm). By comparison, specimens with deeper RDP did not show such features, indicating strong mass transfer processes in downstream plane of local area of the shallow pit. In sum, the mass transfer process of shallow RDP front part can promote deepening of the pit. Also, the mass transfer process in the pit may inhibit further deepening of the corrosion pit as it developed a certain depth. Thus, Re peak at downstream of the

shallow pit would promote formation of new corrosion pits through strong mass transfer processes in surrounding local area of the pit.

In Fig. 11a, RDP upstream vertical wall showed a peak located in middle of the wall, mainly induced by the large vortex inside RDP and leading to enhanced mass transfer process at this position. Therefore, corrosion pits under the flow tended to expand upstream and toward the inside of RDP.

As shown in Fig. 12a, Re at RDP downstream vertical wall decreased with depth of the vertical wall but gradually increased with RDP depth. This indicated that gradual weakening of mass transfer processes in the downstream vertical walls from top to bottom of pit. Hence, downstream walls tended to develop at inclined surface extending downstream.

4.2.2 Mass transfer of reaction product

Corrosion scale composed of $FeCO_3$ would form on X80 pipeline steel surfaces during corrosion processes. The deposited corrosion scale would prevent direct contact between the metal and solution. Hence, ions must be transferred through the corrosion scale through diffusion mass transfer. The metal mass loss rate \dot{m}_{Fe} at metal–corrosion scale interface can be described by Eq. (17) [48]:

$$\dot{m}_{Fe} = \frac{dm_{Fe}}{dt} = K_r \theta_{FeCO_3,ads} (C_e - C_0) \quad (17)$$

where $\frac{dm_{Fe}}{dt}$ is the mass change of Fe in unit time; $\theta_{FeCO_3,ads}$ is the porosity of formed $FeCO_3$ scale; C_e is the solubility of $FeCO_3$; C_0 is the actual concentration of $FeCO_3$ at metal–corrosion scale interface; and K_r is the reaction rate constant.

Some Fe^{2+} will be transported to the solution by diffusion and convection mass transfer. Thus, fraction f (representing the ratio of Fe^{2+} converted into $FeCO_3$ and then deposited) should be introduced. The other part of Fe^{2+} transported to the bulk solution could be expressed as $1 - f$. The diffusion process of metal surface in the corrosion scale would mainly use the micro-pores of corrosion scale as mass transfer channels. The diffusion at stable corrosion scale can be described according to Eq. (18):

$$(1 - f)\dot{m}_{Fe} = \frac{D_{Fe^{2+}} \theta_{FeCO_3,ads}}{\delta_{FeCO_3,ads}} (C_0 - C_1) \quad (18)$$

where $\delta_{FeCO_3,ads}$ is the thickness of the corrosion scale; C_1 is the concentration of Fe^{2+} at corrosion scale–solution interface; and $D_{Fe^{2+}}$ is the diffusion coefficient of Fe^{2+} in corrosion scale given by Eq. (19).

$$D_{Fe^{2+}} = 1.04 \times 10^{-7} T / \mu_s \quad (19)$$

where μ_s is viscosity of the solution; and T is temperature of the solution.

Note that Fe^{2+} ions would then be transported from the corrosion scale–solution interface to bulk solution by convection following Eq. (20):

$$(1 - f)\dot{m}_{\text{Fe}} = K_{\text{Fe}^{2+}}(C_1 - C_b) \quad (20)$$

where $K_{\text{Fe}^{2+}}$ is the mass transfer coefficient of Fe^{2+} by convection at the corrosion scale–solution interface; and C_b is concentration of Fe^{2+} in bulk solution.

Therefore, the rate of metal loss from the steel surface can be described by Eq. (21):

$$\dot{m}_{\text{Fe}} = \frac{\theta_{\text{FeCO}_3, \text{ads}}(C_e - C_b)}{(1 - f) \left[\frac{\theta_{\text{FeCO}_3, \text{ads}}}{D_{\text{Fe}^{2+}}} + \frac{1}{K_{\text{Fe}^{2+}}} \right] + \frac{1}{K_r}} \quad (21)$$

where $D_{\text{Fe}^{2+}}$ is related to the reaction temperature only; and C_e and C_b are associated with the solution and material only. f is considered as 0.5.

$\theta_{\text{FeCO}_3, \text{ads}}$ and $K_{\text{Fe}^{2+}}$ would control the diffusion mass transfer rate of Fe^{2+} at the corrosion scale, as well as interact with the formation of corrosion scale during flow. K_r will also influence the corrosion reaction but be controlled by the reaction conditions.

The micro-pores in corrosion scale would directly affect the diffusion mass transfer process as micro-channels of diffusion mass transfer. Under local flow, corrosion scale with different densities was formed in various regions of the test surface, where corrosion scale looked even destroyed in some areas (Fig. 8). In EIS results, specimens with depths of 0.3, 1.2 and 1.5 mm showed damaged corrosion scale with smaller charge transfer resistances (Fig. 5). Hence, surfaces showed higher mass transfer rates for the corrosion scales with bigger porosity, as confirmed by corrosion rate results (Fig. 7). On the other hand, the mass transfer process in corrosion scale will not be affected under flow but diffusion mass transfer will be influenced by flow at the microstructure level of the corrosion scale.

4.3 Mechanical effect of flow on corrosion scale

In addition to affecting mass transfer and porosity of corrosion scale, flow also affects the integrity of the corrosion scale. To this end, complete and dense FeCO_3 corrosion scale formed may block ion transfer and protect the metal matrix effectively. However, partial destruction of complete and dense corrosion scale under the mechanical action will accelerate the corrosion process of damaged areas. Reported studies showed mainly two mechanical mechanisms of corrosion scale damaged under flow: wall shear stress and cavitation.

Fluids flowing in pipes should slow down by the static solid wall surfaces due to viscosity. Therefore, velocity

gradient should be formed in the vertical direction to that of the flow, and WSS can be described according to Eq. (22) [49]:

$$\tau = \mu \frac{du}{dy} \quad (22)$$

where $\frac{du}{dy}$ is the velocity gradient of the vertical wall.

WSS distribution near the horizontal wall depicted an increase at both upstream and downstream turn points of RDP (Fig. 10b). As RDP depth rose, the peak point of RDP internal WSS moved downstream and the peak data were reduced. At RDP depth of 0.6 mm, the distribution of WSS in the pit was stable mostly.

The distributions of WSS near RDP upstream vertical wall displayed increase in WSS peak with RDP depth. However, RDP upstream vertical wall was located in the negative pressure region with maximum WSS peak of only 36.5 Pa. The latter could not produce enough WSS to the corrosion scale.

WSS distribution on the vertical wall downstream of RDP also illustrated increase in WSS peak with RDP depth. For instance, WSS peak at depth of 1.5 mm was recorded as 164.5 Pa. This value was much higher than that obtained at RDP upstream vertical wall.

The results of EIS (Figs. 5 and 6) and SEM (Fig. 8) revealed the formation of complete corrosion scale in all regions of the surface at RDP depths of 0.6 and 0.9 mm. This demonstrated that WSS was insufficient to destroy the corrosion scale. As RDP further deepened to 1.2 and 1.5 mm, the corrosion scale was destroyed by WSS with damaged area located inside RDP due to the maximum WSS at RDP downstream vertical wall. At RDP depth of 0.3 mm, WSS value looked much smaller than that of other specimens but EIS and SEM still showed destruction of the corrosion scale due to cavitation.

Cavitation would mainly be caused by sudden changes of pressure in flow field. The bubbles will be induced due to the vaporization of liquid phase at low-pressure position. On the other hand, gas dissolved in liquid at low pressure could lead to the collapsed bubbles after recovery of the pressure. The mechanical strength produced by cavitation can reach 10^5 – 10^6 kPa, which is enough to induce destructive effect on the corrosion scale sufficiently.

The absolute pressure distribution showed dramatic changes in horizontal wall and downstream vertical wall at RDP depth of 0.3 mm. Note that the horizontal wall located at the turn point of RDP downstream showed an increase in pressure to 99,195.9 Pa, then suddenly dropped to 90,296.4 Pa and stabilized at 95,000 Pa in the plane of RDP downstream. The vertical near-wall surface on downstream of RDP from top to bottom, showed raise with pressure from the lowest point of 93,702.5 up to 99,520.3 Pa. As depth rose, the pressure improved to more

than 91,000 Pa. The variation in pressure at the horizontal wall was estimated to about 9000 Pa and that of RDP downstream vertical wall was about 6000 Pa. However, under the condition in this experiment, minimum pressure point should be insufficient to vaporize water and form bubbles. Therefore, the formation of bubbles was due to the release of dissolved gas from the solution.

On the other hand, the dissolved carbon dioxide in CO₂-saturated NACE solution should be present in unstable states. Hence, the sudden change in pressure of flow field would release CO₂ [50, 51], leading to formation of CO₂ bubbles movement with the flow. In turn, collapse impact of CO₂ bubbles with the wall in pressure recovery zone would form cavitation. EIS (Figs. 5 and 6) and SEM (Fig. 8) showed formation of complete corrosion scale for specimens with RDP depths of 0.6 and 0.9 mm, indicating occurrence of no cavitation. The fluctuations in surface pressure of specimens with depths of 1.2 or 1.5 mm looked smaller than those of specimens with RDP depths of 0.6 and 0.9 mm. This led to no cavitation and only specimens with RDP depth of 0.3 mm presented cavitation. Thus, CO₂ was released from CO₂-saturated NACE solution at pressure fluctuations around 9000 Pa. According to pressure distribution in specimen with RDP depth of 0.3 mm (Fig. 10), the area with cavitation damage should be in downstream plane of RDP (SEM images in Fig. 8).

5 Conclusions

1. At RDP depth of 0.3 mm, the vertical wall WSS on both sides of RDP was low and insufficient to damage the corrosion scale. However, CO₂ was released and then collapsed at pressure recovery area as pressure dropped in RDP downstream turn point around 9000 Pa. Cavitation caused impact and damage to the corrosion scale, leading to corrosion increase in RDP downstream plane.
2. At RDP depths of 0.6 and 0.9 mm, WSS was insufficient to destroy the corrosion scale. Meanwhile, pressure fluctuation was not enough to release CO₂ and form cavitation. This led to formation of complete and dense corrosion scale covering the entire surface.
3. At RDP depths of 1.2 and 1.5 mm, the pressure fluctuation was insufficient to release CO₂ and form cavitation. However, WSS at RDP downstream vertical wall was enough to destroy the corrosion scale. Thus, corrosion was mainly located in the interior of RDP.

Acknowledgements This work was financially supported by the National Natural Science Foundation of China (Nos. 51774314 and 42176209), Natural Science Foundation of Shandong Province (No.

ZR2021MD064), Fundamental Research Funds for the Central Universities (No. 19CX05001A), and the Key Research and Development Program of Shandong Province (No. 2019GHY112065).

References

- [1] V.V. Zav'Yalov, *Protection Met.* 39 (2003) 274–277.
- [2] Y. Kisaka, N. Senior, A.P. Gerlich, *Metall. Mater. Trans. A* 50 (2019) 249–256.
- [3] D. Jung, J. Kwon, N. Woo, Y. Kim, M. Goto, S. Kim, *Metall. Mater. Trans. A* 45 (2014) 654–662.
- [4] S. Nestic, W. Sun, *Shreir's Corrosion* (2010) 1270–1298.
- [5] Z. Zhu, Y. Cheng, B. Xiao, H.I. Khan, H. Xu, N. Zhang, *Energy* 175 (2019) 1075–1084.
- [6] P.C. Okonkwo, S. Grami, S. Murugan, S. Khan, *J. Iron Steel Res. Int.* 27 (2020) 691–701.
- [7] H. Guo, G.F. Li, X. Cai, J.J. Zhou, W. Yang, *J. Mater. Sci. Technol.* 21 (2005) 33–38.
- [8] G.A. Zhang, Y.F. Cheng, *Corros. Sci.* 51 (2009) 1589–1595.
- [9] Z.W. Tan, L.Y. Yang, D.L. Zhang, Z.B. Wang, F. Cheng, M.Y. Zhang, Y.H. Jin, *J. Mater. Sci. Technol.* 49 (2020) 186–201.
- [10] W. Li, B. Brown, D. Young, S. Nešić, *Corrosion* 70 (2014) 294–302.
- [11] T. Tran, B. Brown, S. Nestic, B. Tribollet, *Corrosion* 70 (2014) 223–229.
- [12] L. Zeng, G.A. Zhang, X.P. Guo, C.W. Chai, *Corros. Sci.* 90 (2015) 202–215.
- [13] G.A. Zhang, L. Zeng, H.L. Huang, X.P. Guo, *Corros. Sci.* 77 (2013) 334–341.
- [14] L. Zeng, G.A. Zhang, X.P. Guo, *Corros. Sci.* 85 (2014) 318–330.
- [15] E. Barmatov, T. Hughes, M. Nagl, *Corros. Sci.* 92 (2015) 85–94.
- [16] X. Tang, L.Y. Xu, Y.F. Cheng, *Corros. Sci.* 50 (2008) 1469–1474.
- [17] S. Nestic, *Energy Fuels* 26 (2012) 4098–4111.
- [18] H.J. Kim, K.H. Kim, *Nuclear Engineering & Design* 301 (2016) 183–188.
- [19] W. Liang, X. Pang, K. Gao, *Corros. Sci.* 136 (2018) 339–351.
- [20] Z.B. Wang, Y.G. Zheng, J.Z. Yi, *Tribol. Int.* 133 (2019) 67–72.
- [21] F.M. Song, *Electrochim. Acta* 55 (2010) 689–700.
- [22] G.A. Zhang, Y.F. Cheng, *Corros. Sci.* 52 (2010) 2716–2724.
- [23] S. Zhang, L. Hou, H. Wei, Y. Wei, B. Liu, *Mater. Corros.* 69 (2017) 1123–1130.
- [24] F.F. Eliyan, A. Alfantazi, *Corrosion* 70 (2014) 880–898.
- [25] H.M. Ezuber, A.A. Shater, *Desalination Water Treatment* 57 (2016) 6670–6679.
- [26] G.A. Zhang, Y.F. Cheng, *Corros. Sci.* 51 (2009) 87–94.
- [27] A. Dugstad, *NACE Int.* 98 (1998) NACE-98031.
- [28] N. Sridhar, D.S. Dunn, A.M. Anderko, M.M. Lencka, U. Schutt, *Corrosion* 57 (2001) NACE-01030221.
- [29] J.M. Pietralik, *E-J Adv. Mainten.* 4 (2012) 63–78.
- [30] W.H. Ahmed, M.M. Bello, M.E. Nakla, A.A. Sarkhi, *Nucl. Eng. Des.* 252 (2012) 52–67.
- [31] T. Yamagata, A. Ito, Y. Sato, N. Fujisaw, *Exp. Therm. Fluid Sci.* 52 (2014) 239–247.
- [32] Y.Z. Xu, M.Y. Tan, *Corros. Sci.* 151 (2019) 163–174.
- [33] M.E. Olvera-Martínez, J. Mendoza-Flores, J. Genesca, *J. Loss Prevention Process Ind.* 35 (2015) 19–28.
- [34] T.J. Harvey, J.A. Wharton, R.J.K. Wood, *Tribol. Mater. Surf. Interf.* 1 (2007) 33–47.
- [35] X. Jiang, Y.G. Zheng, W. Ke, *Corros. Sci.* 47 (2005) 2636–2658.
- [36] L.R.M. Ferreira, H.A. Ponte, L.S. Sanches, A. Abrantes, *Mater. Res.* 18 (2015) 245–249.
- [37] G.D. Eyu, G. Will, W. Dekkers, J. MacLeod, *Appl. Surf. Sci.* 357 (2015) 506–515.

- [38] Z.W. Tan, D.L. Zhang, L.Y. Yang, Z.B. Wang, F. Cheng, M.Y. Zhang, Y.H. Jin, S.D. Zhu, *Tribol. Int.* 146 (2020) 106145.
- [39] L. Zeng, S. Shuang, X.P. Guo, G.A. Zhang, *Corros. Sci.* 111 (2016) 72–83.
- [40] D. Zheng, D. Che, Y. Liu, *Corros. Sci.* 50 (2008) 3005–3020.
- [41] F. Farelas, M. Galicia, B. Brown, S. Nestic, H. Castaneda, *Corros. Sci.* 52 (2010) 509–517.
- [42] N. Buzgar, A.I. Apopei, *Geologie Tomul. L.* 55 (2009) 97–112.
- [43] T.F. Cooney, E.R.D. Scott, A.N. Kort, S.K. Sharma, A. Yamaguchi, *American Mineral.* 84 (1999) 1569–1576.
- [44] A. Isambert, T. De Resseneguiet, A. Gloter, B. Reynard, F. Guyot, J.P. Valet, *Earth Planetary Sci. Lett.* 243 (2006) 820–827.
- [45] A. Kahyarian, M. Singer, S. Nestic, *J. Nat. Gas Sci. Eng.* 29 (2016) 530–549.
- [46] C. Cuevas-Arteaga, J. Uruchurtu-Chavarín, J. Porcayo-Calderon, G. Izquierdo-Montalvo, J. Gonzalez, *Corros. Sci.* 46 (2004) 2663–2679.
- [47] B. Poulson, *Corros. Sci.* 30 (1990) 743–746.
- [48] M. Prasad, V. Gopika, A. Sridharan, S. Parada, *Prog. Nucl. Energy* 107 (2018) 205–214.
- [49] L. Wei, B.F.M. Pots, B. Brown, K.E. Kee, S. Nestic, *Corr. Sci.* 110 (2016) 35–45.
- [50] H.Y. Lin, B.A. Biancucci, S. Deutsch, A.A. Fontaine, J.M. Tarbell, *J. Biomech. Eng.* 122 (2000) 304–309.
- [51] A. Vogel, W. Lauterborn, R. Timm, *J. Fluid Mech.* 206 (2006) 299–338.